Design and Experimental Assessment of a Multi-spherical Composite- Overwrapped Pressure Vessel for Cryogenic Storage

Tapeinos, Ilias; Rajabzadeh, Aydin; Zarouchas, Dimitrios; Groves, Roger; Koussios, Sotiris; Benedictus, Rinze

Publication date
2018

Document Version
Accepted author manuscript

Published in
Conference: ECCM18 - 18th European Conference on Composite Materials

Citation (APA)
Tapeinos, I., Rajabzadeh, A., Zarouchas, D., Groves, R., Koussios, S., & Benedictus, R. (2018). Design and Experimental Assessment of a Multi-spherical Composite- Overwrapped Pressure Vessel for Cryogenic Storage. In V. Kostopoulos (Ed.), *Conference: ECCM18 - 18th European Conference on Composite Materials : Athens, Greece*

Design and Experimental Assessment of a Multi-spherical Composite-Overwrapped Pressure Vessel for Cryogenic Storage

Ilias G. Tapeinos[1], Aydin Rajabzadeh[1], Dimitrios S. Zarouchas[1], Roger M. Groves[1], Sotiris Koussios[1] and Rinze Benedictus[1]

[1]Structural Integrity & Composites Group, Faculty of Aerospace Engineering, Delft University of Technology, Kluyverweg 1, 2629HS Delft, Netherlands

Abstract

In the field of cryogenic storage, the medium inside the pressure vessel is in a liquid state and thus is incompressible. Therefore the storage tank should be designed in a way, that makes the best possible use of the available space within an aircraft. A composite-overwrapped pressure vessel (COPV) based on intersecting spheres (multi-sphere) provides a more volumetrically efficient solution compared to packed cylinders when fitted in a rectangular prescribed box. Additionally, it leads to weight savings due to equal membrane strains when subjected to uniform pressure and less required thermal insulation attributed to the spheres consisting of minimum surface area per given volume. The latter is the result of the minimization of passive heat in the cryogenic liquid and is associated with the fact that spheres have the minimum surface area for a given volume.

In the present work, a numerical and experimental study of a novel multi-spherical COPV with a plastic liner was performed. A thermo-mechanical model based on Finite Element Analysis (FEA) was developed to assess the effect of cryogenic operation at the structure. The model incorporated the dependency of engineering properties and coefficient of thermal expansion of the composite overwrap and liner materials to temperature, in order to describe the structural response to cryogenic temperatures more accurately. This dependency was determined through using approximation functions based on results from material coupon testing. The temperature profile and strain response of the tank were assessed through thermocouples and Fiber Bragg Gratings (FBGs) respectively, throughout the cryogenic chill-down and pressure cycling test. The experimental results verified the accuracy of the involved stiffness and coefficient of thermal expansion (CTE) functions and the FE analysis with average offset of 10 [%]. The most important outcome from the study is the absence of damage in the composite overwrap after cryonic chill-down and pressure cycling, which can be regarded as a positive indication of the suitability of Type IV multi-spherical COPVs for cryogenic storage applications.

1 Introduction

Liquid hydrogen (LH_2) is considered as a strong candidate for a future aviation fuel due to its high gravimetric energy density ([MJ/kg]), making it ideal for long duration flights [1][2]. Additionally, the volumetric energy density ([MJ/l]) of LH_2 is twice as high as gaseous hydrogen (GH_2). The most crucial requirements for LH_2 tanks are the following [3]: i) storage of large volumes, ii) efficient conformation to a given space within the aircraft, iii) operation at cryogenic conditions and iv) small surface area/volume ratio which reduces cryogenic propellant boil-off. It was shown in the Cryoplane Project [4] that cylindrical pressure vessels are not always the optimal configurations for fuel containment, since they result in a considerable unused volume within an aircraft. Haaland [5] showed that multi-cell configurations result in higher volumetric efficiency over packed cylinders when fitted in a prescribed rectangular envelope. The use of a multi-lobe geometry with intersecting conical cells was reported in the LH_2 tank of the X33 vehicle [6]. However in places where the aspect ratio of the enclosing box is closer to 1, the most volumetrically efficient solution is the multi-sphere. A multi-

spherical pressure vessel introduces weight savings, associated with equal membrane strains when subjected to uniform pressure. Additionally, spheres have the minimum surface area for a given volume, which leads to passive heat minimization and thus minimal fuel boil-off.

A novel composite overwrapped multi-spherical tank configuration with a polymer liner was reported in [7]. The tank consisted of four spheres partially merged, with uni-directional (UD) carbon fiber straps applied at the merging points to introduce strain compatibility between the spheres and intersections as well as a central hollow tube in which the fiber straps would pass through.

In this work, an evaluation has been made of the thermo-mechanical performance of the innovative Type IV multi-spherical tank -when subjected to cryogenic storage- using a Finite Element (FE) model. The dependency of the tank wall materials' mechanical properties on temperature was addressed through coupon testing and approximation functions. This served as an input to numerical simulations for the prediction of the material response over the entire temperature range. An experimental verification of the numerical results was performed by pressure cycling a manufactured multi-sphere at cryogenic temperatures. Strain and temperature measurements were performed at the overwrap surface by Fiber Bragg Gratings (FBGs) and thermocouples respectively.

2 Structural Configuration

The multi-spherical COPV of interest can be seen in Fig. 1. It incorporates a plastic liner (PA12) and composite overwrap with a quasi-isotropic (QI) lay-up at the sphere due to equal in-plane stiffness. UD straps were introduced at the sphere connecting areas (junctions) to match the radial expansion of the spheres under internal pressure.

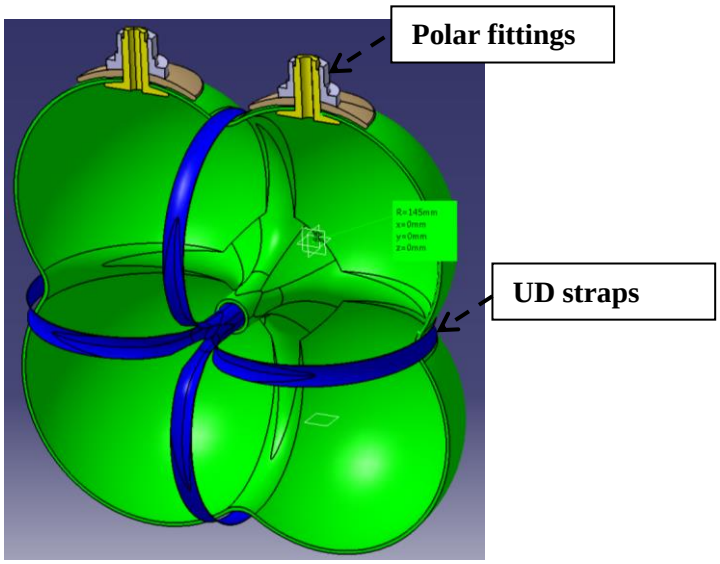

Fig. 1: Multi-spherical COPV with UD straps at the junctions.

The different steps that were carried out for the development of the multi-spherical COPV are illustrated in Fig. 2. Initially, a trade-off study between draping composite patches and structural performance was conducted, where the goal was to identify a composite patch shape that would minimize in-plane shearing of the fabric during draping on the tank contour. The patch shape that would lead to a uniform strain response at the spheres was isolated. Additionally, the required number of UD straps to introduce an equal strain condition between the spheres and intersections was evaluated. Finally draping and curing stages were performed to manufacture the multi-sphere.

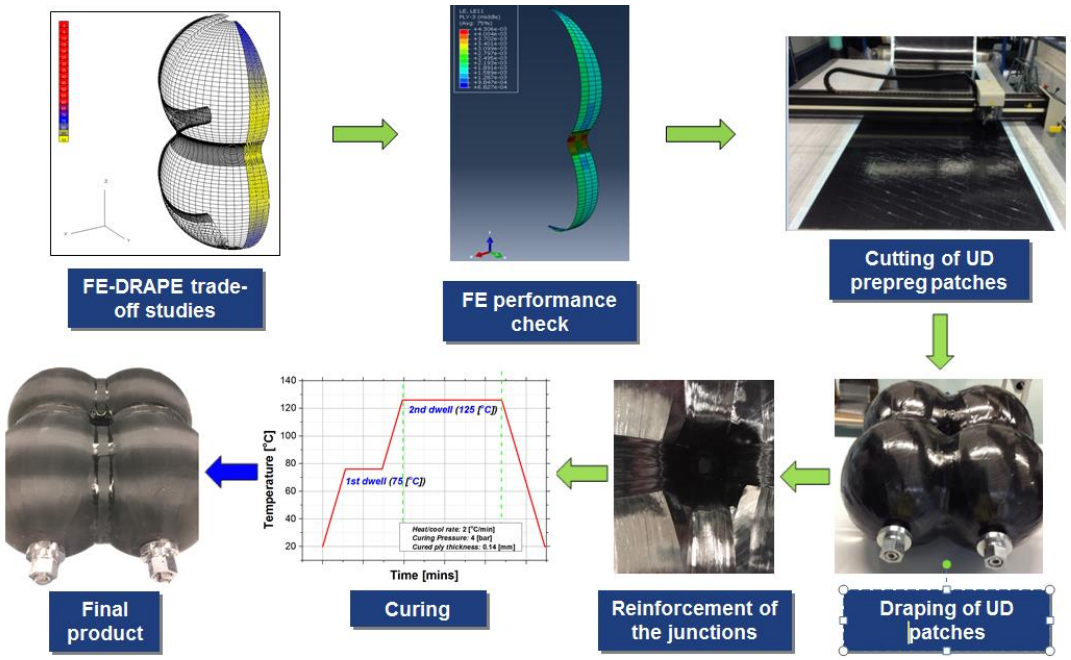

Fig. 2: Development of a multi-spherical COPV.

3 Material Temperature Sensitivity

Uniaxial tensile and compression loading were performed at coupon level at the tank wall constituents (composite overwrap, liner) for various temperatures in accordance to ASTM 3039 [8] and ASTM 6641 [9] standards. The laminate specimen lay-ups were $[0^o]_8$, $[+/-45^o]_{2s}$, $[90^o]_{16.}$ Composite strips were cut with dimensions 250 [mm] x 25 [mm] x 1.12 [mm] or 250 [mm] x 25 [mm] x 2.24 [mm]. The liner samples consisted of a dog-bone geometry in accordance with ASTM 638 [10].

The obtained ply engineering properties (E_{11}: longitudinal modulus, E_{22}: transverse modulus, G_{12}: in-plane shear modulus, ν_{12}: major Poisson's ratio) can be seen in Table 1. Additionally the strength allowables (X_t: longitudinal tensile strength, X_c: longitudinal tensile strength, Y_t: transverse tensile strength, Y_t: transverse compressive strength, S: in-plane shear strength) (ε_{xt}: ultimate longitudinal strain, ε_{yt}: ultimate transverse strain) as well as thermal conductivity values (k_{11}: parallel to the fibers, k_{22}: transverse to the fibers) are given below.

Table 1: CFRP ply properties at various temperatures.

T [°C]	E_{11} [GPa]	E_{22} [GPa]	ν_{12} [-]	G_{12} [GPa]	X_t [MPa]	X_c [MPa]	Y_t [MPa]	Y_c [MPa]	S [MPa]	ε_{xt} [%]	ε_{yt} [%]	k_{11} [W/mK]	k_{22} [W/mK]
-269	137.8**Fout! Verwijzingsbron niet gevonden.**	10.8[13]	-	6.93 [12]	2289**Fout! Verwijzingsbron niet gevonden.**	1202[12]	84.3[12]	314.1[12]	98.3[12]	-	-	-	-
-40	132.8	10.4	0.251	5.6	2186	1193	79.3	278.3	80.2	1.54	0.73	-	-
-10	131.7	9.7	0.272	5.2	2125	1181	75.3	253.2	74.8	1.61	0.77	-	-
23	128.6	8.6	0.278	4.7	2067	1130	67.1	244.7	71.6	1.65	0.81	4.11	0.735
125	126.5[12]	≈0	-	≈0	2007[12]	≈0	≈0	≈0	≈0	-	-	-	-

The values for the Young's modulus (E), Poisson's ratio (ν_{12}), ultimate tensile strength (UTS), elongation at break (ε_{ult}) and thermal conductivity (k) of the liner material (PA12) that were obtained experimentally at different temperatures are given below (Table 2).

Table 2: PA12 properties at various temperatures.

T [ºC]	E [GPa]	ν_{12} [-]	UTS [MPa]	ε_{ult} [%]	k [W/mK]
-269	6.9[14]	-	117.2[15]	-	-
-70	3.8	0.34	77.6	3.87	-
-40	2.9	0.34	69.3	5.51	-
-10	2.4	0.39	63.5	8.23	-
23	1.5	0.41	43.3	19.3	0.365
60	0.7	0.43	36.2	45.4	-
90	0.5	0.45	25.4	126.4	-
125	0.3[14]	-	16.1[15]	-	-

The above experimental results were utilized as data points to extrapolate over a wider temperature range using a least squares fit approach. Approximation functions with some physical basis were sought, that would behave reliably inside and outside of the experimental data points. The temperature extremes of interest were liquid Helium boiling point (T_1 = -269 [ºC]) and the curing temperature of the composite overwrap (T_2 = 125 [ºC]). A separate set of fitting constants {*a*, *b*, *c*} was assigned to every fitting function. These constants were derived from applying the least squares fit method to the experimental results.

The approximation functions used for the liner and composite overwrap materials can be seen in Table 3. A hyperbolic function was utilized for the case of the elongation at break of the liner material (PA12) since a close-to-zero value is expected at cryogenic temperatures while a considerable value is expected at temperatures higher than the glass transition temperature (T_g), as material softening occurs. The stiffness and strength of the liner and overwrap can be approximated by a sigmoid function (Eqn. 2), due to the asymptotic behaviour expected at high and low temperatures as well as the viscoelastic response of the materials at the temperature range of interest. In this case *a* represents the unrelaxed value of that property at absolute zero temperature (-273 [ºC]) while *b* and *c* were associated here with the increasing stiffness/strength trend. Additionally, the CTE of the composite ply at [0º] (α_{11}^{T}) and [90º] (α_{22}^{T}) orientations and the liner material (α_{liner}^{T}) was approximated using a polynomial fit of a third order (a T^3 dependence exists in crystalline polymers - according to Hartwig [16]).

Table 3: Approximation functions for the liner and overwrap materials.

A/A	Property	Function
(1)	$\varepsilon_{ult\_liner}^{T}$	$f(a,b,c\,|\,T) \Rightarrow \frac{1}{(a-bT)^{c}}$
(2)	$E_{liner}^{T}, E_{11}^{T}, E_{22}^{T}, G_{12}^{T}$ $UTS_{liner}^{T}, X_{t}^{T}, X_{c}^{T}, Y_{t}^{T}, Y_{c}^{T}, S^{T}$	$f(a,b,c\,|\,T) \Rightarrow \frac{a}{(1+be^{-cT})}$
(3)	ε_{xt}^{T} , ε_{yt}^{T}	$f(a,b,c\,|\,T) \Rightarrow \frac{X_{t}^{T}}{E_{11}^{T}}$, $f(a,b,c\,|\,T) \Rightarrow \frac{Y_{t}^{T}}{E_{22}^{T}}$
(4)	$\alpha_{liner}^{T}, \alpha_{11}^{T}, \alpha_{22}^{T}$	$f(a,b,c,a^{o}\,|\,T) \Rightarrow aT^3 + bT^2 + cT + \alpha^{o}$

The best-fit values for the coefficients *α*, *b*, *c* and α^{o} of all the approximation functions are outlined below. It is evident that higher *b* and *c* values were obtained for the matrix-dominated properties ($E_{22}^{T}, G_{12}^{T}, X_{c}^{T}, Y_{t}^{T}, Y_{c}^{T}, S^{T}$).

Table 4: Fitting constants of approximation functions.

Property	Unit	a [-]	b [-]	c [-]	a^{o} 10^{-6} [mm/mm ºC]

$\varepsilon^{T}_{ult\_liner}$	[%]	0.36	0.0026	2.36	-
E^{T}_{liner}	[GPa]	7.009	2.797	-0.0181	-
UTS^{T}_{liner}	[MPa]	117	1.164	-0.0127	-
α^{T}_{liner}	10^{-6} [mm/mm ^{o}C]	$1.4 \cdot 10^{-12}$	$5.3 \cdot 10^{-10}$	$4.3 \cdot 10^{-7}$	$110.6 \cdot 10^{-6}$
E^{T}_{11}	[GPa]	136.884	0.044	-0.0056	-
E^{T}_{22}	[GPa]	11.202	0.171	-0.0251	-
G^{T}_{12}	[GPa]	6.903	0.353	-0.0273	-
X^{T}_{t}	[MPa]	2372	0.116	-0.0049	-
X^{T}_{c}	[MPa]	1201	0.011	-0.0791	-
Y^{T}_{t}	[MPa]	87	0.145	-0.0231	-
Y^{T}_{c}	[MPa]	314	0.192	-0.0338	-
S^{T}	[MPa]	103	0.387	-0.0254	-
α^{T}_{11}	10^{-6} [mm/mm ^{o}C]	$5 \cdot 10^{-15}$	$4 \cdot 10^{-11}$	$-4.6 \cdot 10^{-10}$	$-0.613 \cdot 10^{-6}$
α^{T}_{22}	10^{-6} [mm/mm ^{o}C]	$2.93 \cdot 10^{-12}$	$8.1 \cdot 10^{-10}$	$0.12 \cdot 10^{-6}$	$32.15 \cdot 10^{-6}$

The composite ply longitudinal and transverse modulus as well as strength as a function of temperature are depicted in Fig. 3. The values of those properties at temperature extremes were obtained from published works, based on results from coupon testing or micro-mechanics approach Table 1Table 2. It can be seen that temperature had a negligible effect in the longitudinal direction since all ply properties are fiber-dominated in that direction. On the other hand, temperature had a significant effect in the transverse direction, since matrix relaxation at elevated temperatures occurs and is responsible for a sudden decrease of the corresponding ply engineering properties. Furthermore, it is evident that the engineering properties obtained higher values at cryogenic temperatures due to closer compaction of polymer molecules and an increase of the binding forces.

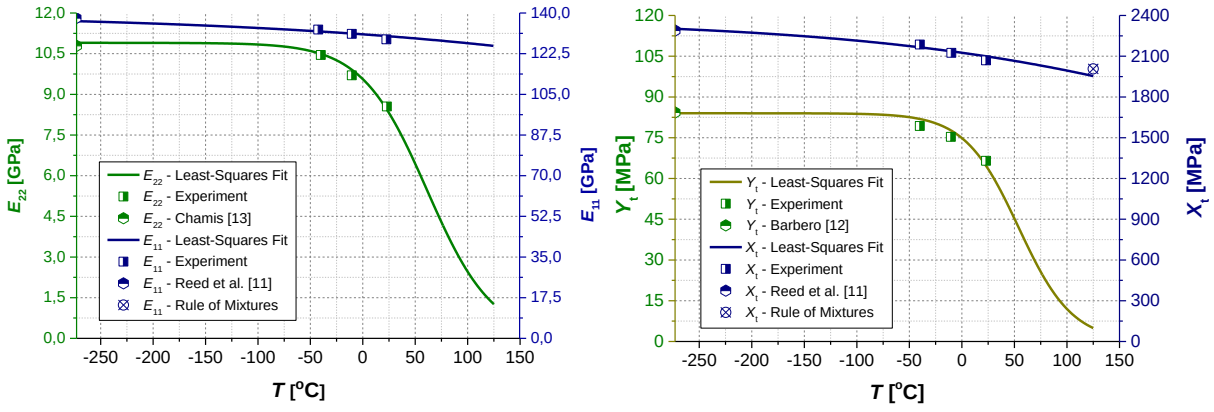

(a) **(b)**

Fig. 3: Ply a) longitudinal and transverse modulus and b) longitudinal and transverse strength as a function of temperature.

The CTE values of the liner and overwrap materials over the temperature range -273 [^{o}C] $\leq$ $T \leq$ 125 [^{o}C] is shown in Fig. 4. A very good agreement (average offset of 3.1[%]) was obtained between

this work and the recordings of Baschek et al. [14] for -196 [°C] ≤ T ≤ -75 [°C] on the CTE values of PA12. The difference in CTE between the liner and the overwrap as well as the difference in CTE along the fiber and the transverse direction within one ply will lead to dissimilar thermal displacements when the tank is exposed to cryogenic chill-down.

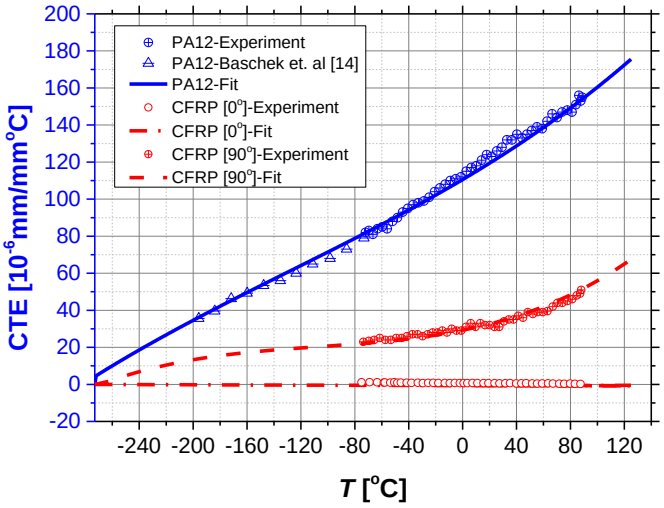

Fig. 4: CTE for the liner (PA12) and overwrap (CFRP) materials.

The approximation functions developed above will be used in the FE analysis (presented below), in order to predict more accurately the response of the tank constituents to cryogenic chill-down and pressure cycling.

4 FE model

The 3D tank structure was imported from the draping simulation software DRAPE to a commercial software package (Abaqus). A local fiber orientation and stiffness was assigned to each ply within every element (associated with in-plane shearing of fibers during draping). The loading steps of the multi-sphere are based on the loads a cryogenic propellant tank is subjected to throughout operation and include: i) curing, ii) cryogenic chill-down (filling to 75 [%] of volume), iii) pressure cycling and iv) tank draining (Fig. 5a). More specifically, the maximum expected operating pressure (MEOP) (at 3.8 [bar]) of the LH_2 tank of the SpaceLiner Reusable Launch Vehicle (RLV) was taken into consideration throughout the numerical simulation [17]. Since the cryogen that would be employed for the experiment would be liquid nitrogen-LN_2 (boiling point: -196 [°C]) instead of LH_2 (boiling point: -253 [°C]) for safety reasons a temperature boundary condition (T_{in} = -196 [°C]) was defined at the inner surface of the liner (Fig. 5b). Additionally, a free convection boundary condition was applied at the liner surface next to the vapour region with a heat transfer coefficient of h_{vapor} = 22.6 [W/m^2 K] and a vapor temperature of T_{vapor} = -123 [°C] in accordance with the work of Stephens [18]. A frost layer on the outside of the tank contour was added due to the lack of thermal insulation resulting in water condensation and freezing. The frost layer thickness and conductivity values were based on [19] and varied along the height direction in accordance with the expected exposure time to LN_2 throughout the experiment. A thermal contact conductance scenario was considered to assess the heat transfer between the liner and the composite overwrap, since an air gap would be formed during chill-down associated with the CTE mismatch of the two tank wall constituents. As a result, heat transfer between the liner and overwrap shells would be a function of the air gap thickness (Fig. 5b).

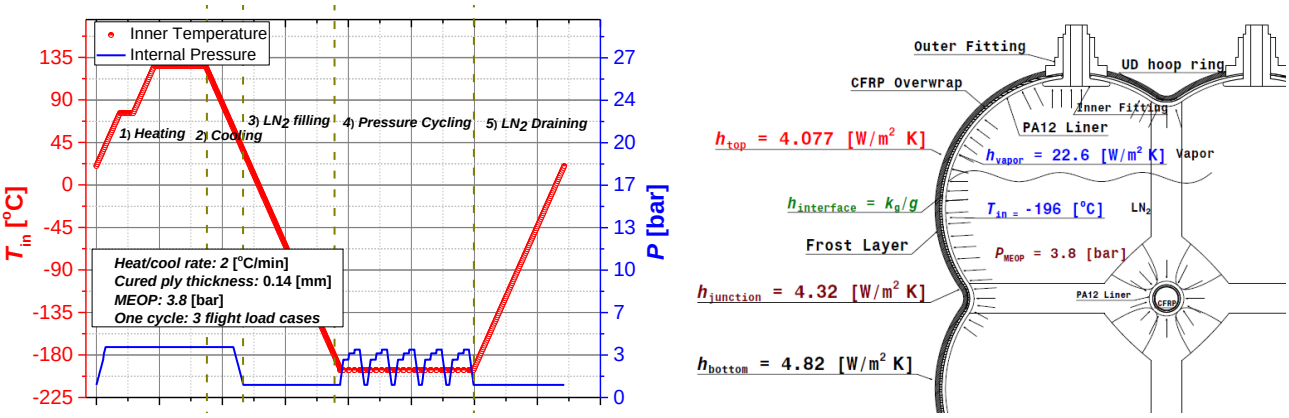

(a) **(b)**

Fig. 5: a) Internal pressure vs inner temperature profile and b) loads and boundary conditions at the tank.

Furthermore a free convection boundary condition was applied at the tank outer surface (Fig. 5b). Assuming that the heat transfer rate is constant in the radial direction, the heat transfer coefficient values at various locations at the outer surface of the tank are obtained by solving the following system of heat conduction equations for h_{out}:

$$q_i = q_j = q_{out} \Rightarrow -kA\left(\frac{dT}{dr}\right)_i = -kA\left(\frac{dT}{dr}\right)_j = h_{out}A\left(T_{out} - T_\infty\right) \quad (5)$$

where subscripts i,j denote thermal conduction in solid surfaces i and j respectively, q is the heat transfer rate, k represents the thermal conductivity of a tank wall constituent, A is the surface area of the shell, r corresponds to the radial direction in the spherical coordinate system and T_{out} and T_∞ are the tank external surface and ambient air temperatures respectively.

5 Tank Testing

5.1. Test Description

Repeated pressure cycling at cryogenic temperatures as well as emptying of the tank represents the multiple filling/draining phases that occur during a tank's lifetime. Assessment of the temperature profile at the tank contour enables the identification of the different heat transfer phenomena occurring at various tank locations. Evaluation of the effect of both temperature and internal pressure on the strain behaviour of the composite overwrap gives an insight on the overall structural response when subjected to operational loads.

5.2. Instrumentation

Fiber Bragg gratings (FBGs) with an Ormocer coating were mounted at different locations at the tank wall surface to evaluate strain throughout the different testing stages (filling with cryogen, pressure cycling, draining). The FBG sensors utilized in this study were LBL-1550-125 draw tower grating (DTG) type sensors (FBGS International NV) with a sensor length of 8 [mm]. The PXIe-4844 optical sensor interrogator (from National Instruments) was used to record the FBG outputs at 10 [Hz]. Furthermore, thermocouples (type K) were bonded to the tank adjacent to every FBG sensor, in order to derive a temperature-strain relationship.

The different locations on the tank surface where FBGs and thermocouples were mounted are illustrated in Fig. 6. Temperature recordings were performed in an additional 3 points (at three different heights along the tank lower sphere). The FBGs were divided into 4 groups based on the different regions of interest: i) spherical cells, ii) top junction and hollow tube, iii) horizontal junction

and hollow tube and iv) polar openings. Every FBG group was assigned to obtain the temperature and strain gradient along a corresponding path at the tank. Temperature and strain gradient along a path can be associated to the varying heat transfer mode relative to the distance from the liquid interface level or to the relative air gap thickness between the liner and the overwrap.

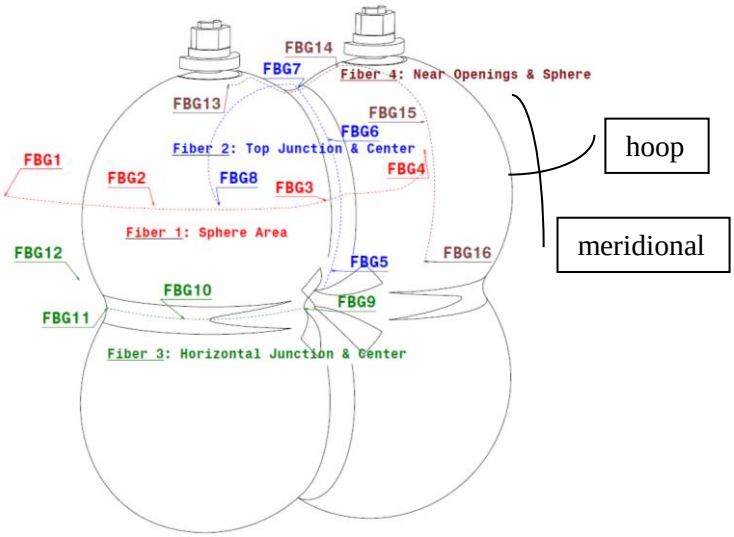

Fig. 6: Layout of the various FBGs at the tank contour.

The experimental setup during the cryogen draining can be seen in Fig. 7. The test tank was supplied with LN_2 under a low pressure (close to ambient) and a pressure relief valve device (set at 5 [bar]) controlled the tank pressure to below a safe level. Pressure was monitored with a pressure gauge that was connected to the pipeline.

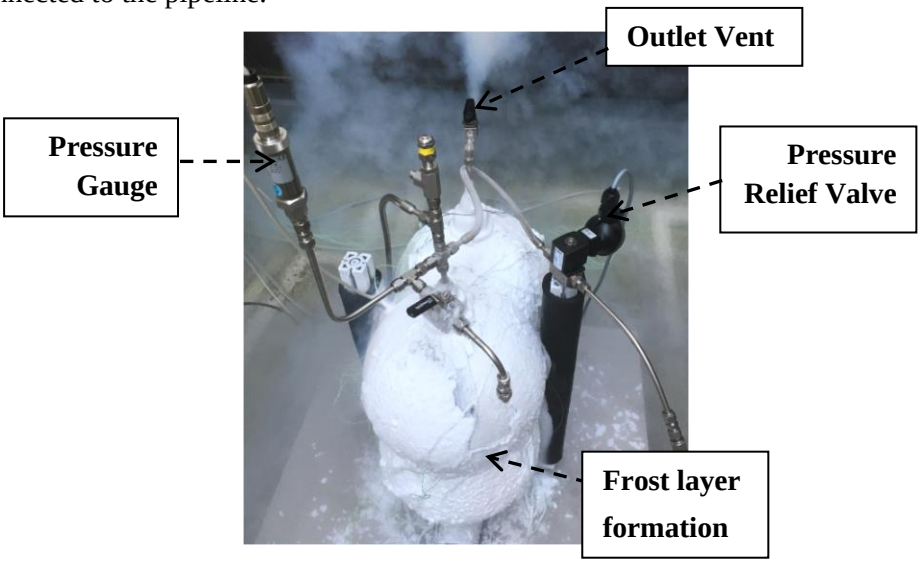

Fig. 7: Overview of the experimental setup at the draining phase.

5.3. Experimental Procedure

The test procedure consisted of the following steps:

i. Filling of the test tank with LN_2 to a level of 75 [%] of its volume (feeding rate 0.0045 [kg/s]).
ii. Stepwise active pressurization (GN_2) to 3 [bar], 3.5 [bar] and 3.8 [bar].
iii. Unloading to atmospheric pressure.
iv. Repetition of steps (ii) and (iii) five times to simulate a number of pressure and temperature cycles.
v. Draining of the tank (under low vacuum 50 [mbar]).

The formation of a frost layer after cryogenic chill-down is depicted in Fig. 7. This can be attributed to cooling of ambient air below its dew point and water vapour condensation.

6 Results

Temperature and meridional strain at the upper sphere (sensor #16 - location can be seen in Fig. 6) as a function of time during the cryogenic test is shown in Fig. 8. The direction of the meridional strain is defined by the revolution axis of every sphere while the hoop direction is always transverse to the meridional direction (Fig. 6). The temperature on the entire tank wall was dictated by any of the following four heat transfer modes:

i) vapor-free convection (at the ullage region),
ii) radial thermal conduction at the vessel walls,
iii) meridional thermal conduction at the vessel walls,
iv) convection associated with LN_2 boiling (at the liquid interface level).

The first three heat transfer modes were the primary mechanisms of wall cooling until 5500 [s] approximately (Fig. 8). Temperature and strain decreased in a non-linear fashion throughout the chill-down phase. From the moment that the cryogen level passed sensor #16 a very sudden temperature decrease was recorded from 5500 [s] to 6000 [s] due to liquid boiling. Throughout steady state conditions stage (6000 [s] < $t \leq$ 10000 [s]) strain and temperature maintained a steady value with the overwrap in this location not reaching LN_2 saturation temperature due to the air gap formed between itself and the liner. Liner cracking occurred at the central cylindrical tube at the end of the chill-down stage (t = 5500[s]). Addition of pressurant (GN_2 at room temperature) led to rapid LN_2 evaporation, which was reflected by the temperature jump and strain increase in Fig. 8.

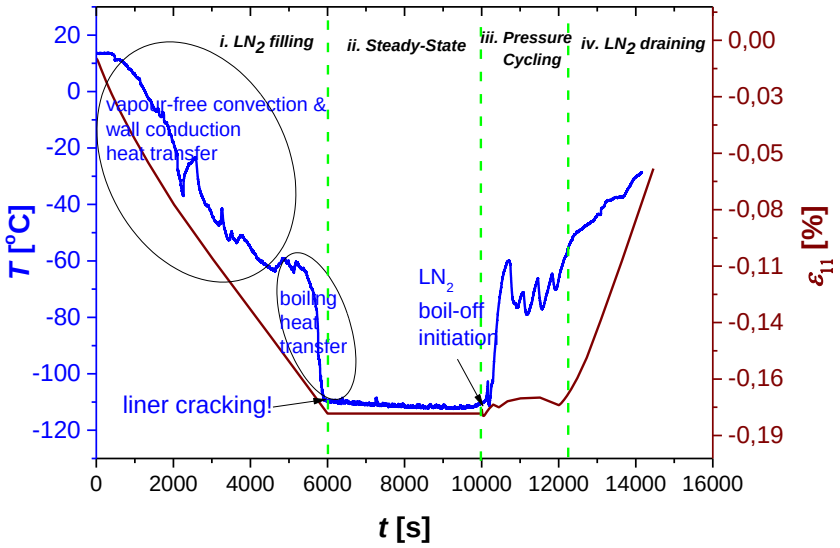

Fig. 8: Temperature and internal pressure history at the upper sphere (sensor 16) versus time.

At this point, it is critical to evaluate strain as a function of temperature and pressure by using the approximation functions presented in Section 3 and to compare this to the findings from experimental measurements. This comparison will allow for a verification of these approximation functions. Strain as a function of temperature and pressure for the QI laminate is given by the following thermo-elastic load-deformation relationship:

$$\boldsymbol{\varepsilon}(T,P)=\begin{Bmatrix}\alpha_{\mathrm{QI}}(T)_{\mathrm{L}}\\ \alpha_{\mathrm{QI}}(T)_{\mathrm{T}}\\ 0\end{Bmatrix}\Delta T+\mathbf{S}_{\mathrm{QI}}(T).\begin{Bmatrix}1\\1\\0\end{Bmatrix}\left(\frac{PR}{2t}\right), \tag{6}$$

$$\text{where } \alpha_{\mathrm{QI}}(T)_{\mathrm{L}}=\alpha_{\mathrm{QI}}(T)_{\mathrm{T}}=\frac{\alpha_{11}^{\mathrm{T}}\left(E_{11}^{\mathrm{T}}+E_{22}^{\mathrm{T}}\nu_{12}\right)+\alpha_{22}^{\mathrm{T}}E_{22}^{\mathrm{T}}\left(1+\nu_{12}\right)}{E_{11}^{\mathrm{T}}+E_{22}^{\mathrm{T}}+2E_{22}^{\mathrm{T}}\nu_{12}} \tag{7}$$

$$\mathbf{S}_{\mathrm{QI}}(T)=\left[\frac{1}{\sum_{k=1}^{n}t_{\mathrm{ply}}}\sum_{k=1}^{n}\mathbf{C}(T,\theta)t_{\mathrm{ply}}\right]^{-1} \tag{8}$$

$$\mathbf{C}(T,\theta)=\mathbf{M}(\theta)\cdot\begin{pmatrix}\frac{E_{11}^{\mathrm{T}}}{1-\nu_{12}\nu_{21}} & \frac{\nu_{12}E_{22}^{\mathrm{T}}}{1-\nu_{12}\nu_{21}} & 0\\ \frac{\nu_{12}E_{22}^{\mathrm{T}}}{1-\nu_{12}\nu_{21}} & \frac{E_{22}^{\mathrm{T}}}{1-\nu_{12}\nu_{21}} & 0\\ 0 & 0 & G_{12}^{\mathrm{T}}\end{pmatrix}\cdot\mathbf{M}^{\mathrm{T}}(\theta) \tag{9}$$

where $\alpha_{\mathrm{QI}}(T)_{\mathrm{L,T}}$ are the CTE coefficients ατ longitudinal and transverse directions of the QI laminate as a function of temperature derived from Miller [20] for the thermally isotropic material case. The parameter $\mathbf{S}_{\mathrm{QI}}(T)$ represents the compliance matrix of the QI laminate as a function of temperature, while $\mathbf{C}(T,\theta)$ is the transformed ply stiffness matrix and $\mathbf{M}(\theta)$ is the transformation matrix. A uniform temperature drop (ΔT) was assumed through the thin-walled overwrap. The engineering constants E_{11}^{T}, E_{22}^{T} and G_{12}^{T} as well as the CTE of the composite ply at the longitudinal (α_{11}^{T}) and transverse (α_{22}^{T}) directions can be found in Section 3.

Meridional strain as a function of temperature is depicted in Fig. 9 for the cases of no added pressure and for P = 2.8 [bar] at the sphere at the ullage region (sensor #15) and below-the-liquid level (sensor #16). A comparison between the results of the FE analysis and experimental recordings for no added pressure is hereby illustrated. As expected, a non-linear relationship (joined effect of sigmoid function and polynomial functions) between meridional strain and temperature can be seen in both Fig. 9a and Fig. 9b linked to the approximation functions. Higher compressive strain values were recorded below-the-liquid level, caused by the larger ΔT at that location. For the case of P = 2.8 [bar] Eqs. (6-9) were utilized, where a tensile meridional strain component is added to the total strain.

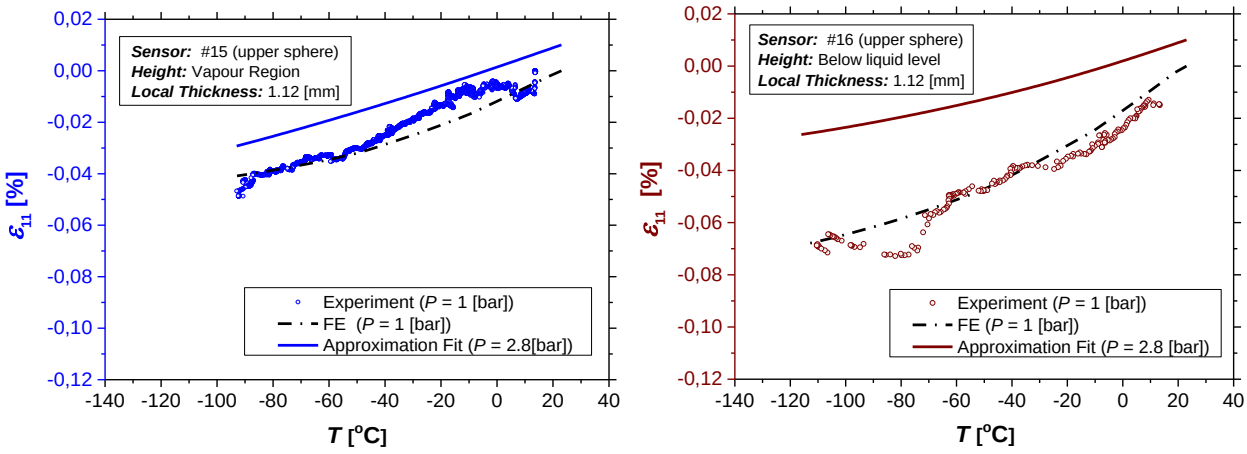

(a) **(b)**

Fig. 9: Correlation between meridional strain and temperature for no added pressure and for *P* = 2.8 [bar] for the sphere at a) ullage region and b) below-the-liquid level for the chill-down stage.

The FE and experimental values for the un-pressurized case showed good agreement with a small offset for -40 [°C] ≤ T ≤ 10 [°C] and -100 [°C] ≤ T ≤ 70 [°C] for sensors #15,16 respectively. As a result the accuracy of the approximation functions and the FE model are verified (with an average offset of 10 [%]).

7 Conclusions

In this work, a numerical and experimental assessment of the thermo-mechanical response of a novel Type IV multi-spherical COPV has been presented. The multi-spherical COPV consisted of four quasi isotropic, merged spherical chambers (scaled to 44 [l]). The tank was subjected to cryogenic chill-down with LN_2 followed by pressure cycling. Strain and temperature measurements were obtained by Fiber Bragg Gratings (FBGs) and thermocouples respectively and the obtained experimental results were employed for a comparison with the FEM-based modelling procedures.

Four different heat transfer modes were obtained at the tank wall during chill-down: i) free convection (at the ullage region), ii) radial thermal conduction, iii) meridional thermal conduction and iv) convection associated with LN_2 boiling (at the liquid interface level). The joined effect of sigmoid (E(T)) and polynomial (CTE(T)) functions leads to a non-linear relationship between meridional strain and temperature, where higher compressive strain values are obtained below-the-liquid level compared to the ullage region, due to larger ΔT. The increase of internal pressure (P = 2.8 [bar]) results in a tensile meridional strain component added to the total strain. Strain recordings at the composite overwrap verified the accuracy (with an average offset of 10 [%]) of the approximation functions for CTE(T) and E(T) and the FE model results for the unpressurized state.

It was however shown that at the end of the cryogenic chill-down stage, liner cracking took place at the central hollow tube due to CTE mismatch between the composite overwrap and the liner materials (PA12). Damage onset in the liner did not influence the structural integrity of the overwrap and no pressure loss was observed.

Future work should aim at the evaluation of different liner materials for a Type IV multi-sphere COPV, to assess whether testing at cryogenic temperatures can be carried out without any damage onset. A liner material with lower CTE and higher ultimate failure strain at cryogenic temperatures, that is suitable for moulding processes that provide better thickness control must be investigated. Furthermore, strain monitoring of the multi-spherical COPV throughout the curing process would be beneficial in terms of the assessing the residual stresses from manufacturing.

References

[1] G.D. Brewer, 'Hydrogen Aircraft Technology', CRC Press, 1991.

[2] A. Westenberger, 'Final Technical Report: Liquid hydrogen fuelled aircraft - system analysis' 2003.

[3] S.K. Mital, J.Z. Gyekenyesi, S.M. Arnold, R.M. Sullivan, J.M. Manderscheid and P.L.N. Murthy, 'Review of Current State of the Art and Key Design Issues With Potential Solutions for Liquid Hydrogen Cryogenic Storage Tank Structures for Aircraft Applications', *NASA/TM-214346*, 2006.

[4] A. Westenberger, 'Liquid hydrogen fuelled aircraft - system analysis. Final Technical Report-CryoPlane Project', GRD1-1999-10014, 2003.

[5] A. Haaland, 'High-Pressure Conformable Hydrogen Storage for Fuel Cell Vehicles', Proceedings of the U.S. DOE Hydrogen Program Review, California, 2000, 463-469.

[6] 'Final Report of the X-33 Liquid Hydrogen Tank Test Investigation', NASA Marshall Space Flight Center, Huntsville, 2000.

[7] I.G. Tapeinos, S. Koussios and R.M. Groves, 'Design and analysis of a multi-cell subscale tank for liquid hydrogen storage', *International Journal of Hydrogen Energy*, **41**, 3676-3688, 2016.

[8] ASTM 3039-02, 'Standard test method for tensile properties of polymer-matrix composite materials', 1995.

[9] ASTM 6641, 'Standard test method for compressive properties of polymer matrix composite materials using a combined loading compression (CLC) test fixture'.

[10] ASTM 638-03, 'Standard test method for tensile properties of plastics', 2003.

[11] R.P. Reed and M. Golda, 'Cryogenic properties of unidirectional composites', *Cryogenics*, **34**, 909-928, 1994.

[12] E.J. Barbero, 'Introduction to Composite Materials Design', Taylor & Francis Group, 1999.

[13] C.C. Chamis, 'Simplified Composite Micromechanics Equations for Hygral Thermal and Mechanical Properties', *SAMPE Quarterly*, 15, 14-23, 1984.

[14] G. Baschek, G. Hartwiga and F. Zahradnik, 'Effect of water absorption in polymers at low and high temperatures', *Polymer*, **40**, 3433–3441, 1991.

[15] Toray Plastics, 'Technical Report-Nylon Plastics'.

[16] G. Hartwig, 'Polymer Properties at Room and Cryogenic Temperatures', *The International Cryogenics Monograph Series*, 1994.

[17] CHATT Project, 'Final Report', 2015.

[18] C.A. Stephens, G.J. Hanna and L. Gong, 'Thermal-Fluid Analysis of the Fill and Drain Operations of a Cryogenic Fuel Tank', NASA Technical Memorandum, 1993.

[19] K-H. Kim, H-J. Ko, K. Kim, Y-W. Kim and K-J. Cho, 'Analysis of heat transfer and frost layer formation on a cryogenic tank wall exposed to the humid atmospheric air', *Applied Thermal Engineering*, **29**, 2072-2079, 2009.

[20] A.K. Miller, 'Thermal expansion coefficients for laminates obtained invariant lamina properties', **13**, *Fiber Science and Technology*, 397-409, 1980.